JOURNAL OF PROPULSION AND POWER
Vol. 15, No. 5, September–October 1999

Methodology for Analysis of Postshock Oscillations During Pulse-Triggered Instability

P. G. Harris*
Defence Research Establishment Valcartier, Val-Bélair, Québec G3J IX5, Canada
and
A. de Champlain†
Université Laval, Québec, Québec G1K 7P4, Canada

Past experimental studies have suggested that the propagating shock wave associated with pulse-triggered instability in solid rocket motors is followed by postshock oscillations. A new methodology was developed to confirm the existence and evaluate the nature of these oscillations. This methodology is composed of a new time-marching frequency and a time-frequency analysis. The new time-marching analysis follows the evolution of the time-averaged frequency content of the postshock oscillations throughout a firing, whereas with the time-frequency analysis, it is possible to obtain a qualitative estimate of the temporal evolution of the amplitude of the frequency content of postshock oscillations for a single shock-wave cycle. The new methodology was developed and tested with model signals and then successfully applied to a sample experimental signal.

Introduction

DURING the operation of solid rocket motors, the passage of ejecta through the nozzle will create a small compression wave, which can grow into a large-amplitude steep-fronted wave (shock wave). This wave is usually accompanied by an increase in the time-averaged operating pressure of the motor. This type of instability, illustrated in Fig. 1, can be referred to as pulse-triggered nonlinear longitudinal combustion instability, identified from here on as pulse-triggered instability.

Considerable experimental investigation of pulse-triggered instability has been carried out at the Defence Research Establishment Valcartier, beginning in the early 1960s with Brownlee[1] and continuing most recently with Harris and de Champlain.[2] This latter work was the Canadian contribution to a joint international program based on an extensive experimental study by Phillips Laboratory and Aerojet Solid Propulsion Company.[3] The work reported by Blomshield et al.[4] was part of the American contribution to this joint program.

The above-mentioned experimental studies, for the most part, concentrated on the amplitude and the modal composition of the shock wave. However, close examination of the experimental data reveals interesting postshock oscillations, as seen in Fig. 2, which is an expanded view of the data in Fig. 1. These oscillations, which have often been explained by transducer ringing, were attributed to various acoustic or structural modes of vibrations[5,6] by the present authors. However, the standard methodology used for the frequency analysis of the experimental data never produced convincing evidence. Recently, this methodology was revisited and modified. The resulting new methodology is composed of what is identified in this paper as time-marching frequency and time-frequency analyses.

The new time-marching analysis is a direct adaptation of standard time-marching fast Fourier transform (FFT) frequency analysis methodology used in the field of combustion instability. With this new time-marching analysis, it is possible to follow the evolution of the time-averaged frequency content of the postshock oscillations throughout a firing. The time-frequency component of the methodology was borrowed from the field of signal processing. With this analysis it is possible to obtain a good qualitative estimate of the temporal evolution of the frequency content of postshock oscillations for a single shock-wave cycle.

This paper provides a detailed description of the new methodology. It begins with the definition of three model signals that are used throughout the paper to illustrate and test the new methodology before its application to the sample experimental signal (Figs. 1 and 2). Next, the standard time-marching analysis is described, and, by use of two model signals, its weaknesses are illustrated and the new analysis is developed. Subsequently the new analysis is applied to the sample experimental signal. The focus then shifts to the discussion of different time-frequency analysis algorithms, with the emphasis placed on their practical application. The frequency and the time resolutions of the algorithms are then explored with all three model signals. The time-frequency analysis discussion is then completed with the application of selected analyses to the sample experimental signal. Finally, conclusions concerning the new methodology are drawn.

Although certain remarks concerning the nature of the postshock oscillations are made throughout the paper, these are only incidental to the primary goal of presenting the analysis methodology. This presentation sets the stage for a detailed analysis of postshock oscillations in subsequent papers.

Model Signals

The approach chosen in the discussion of the new methodology is based on numerical experimentation rather than on rigorous mathematical proof. As such, three model signals are defined at the outset. The characteristics of the signals are specified in Table 1 and illustrated in Figs. 3–5.

Model signal 1, Fig. 3, is 512 points long. For the first 100 points the signal is zero. This is followed by 369 points of a sine wave with a unitary amplitude at a frequency of 11.1 kHz. For the last 43 points the signal is zero. This signal is used to evaluate the ability of different time-frequency algorithms to track the temporal evolution of a constant-amplitude signal.

Model signal 2, Fig. 4, is the simplest approximation of the experimental signal composed of a train of shock waves, each followed by postshock oscillations. The steep-fronted wave at the top of the figure is added to the periodic decaying sine to form the combined signal. The sine frequency and the decay alpha associated with the decaying sine are given in Table 1. The fundamental frequency of the steep-fronted wave, 690 Hz, and the sampling rate, 250 ksamples/s, were the same as for the experimental signal. Both the decaying

Received 5 July 1998; revision received 26 April 1999; accepted for publication 24 May 1999.

*Leader, Propulsion Group, Delivery Systems. Member AIAA.
†Professor, Mechanical Engineering.

Table 1 Specification of the characteristics of the model signals

Model	Frequency, kHz	Decay alpha, s^{-1}	Amplitude
1	11.1	0	1.00
2	9.6	−3000	0.25
3	2.33	−1500	0.15
	4.0	−1500	0.20
	9.6	−1250	0.10
	11.1	−2200	0.65
	23.0	−8800	1.00
	31.0	−2200	0.65

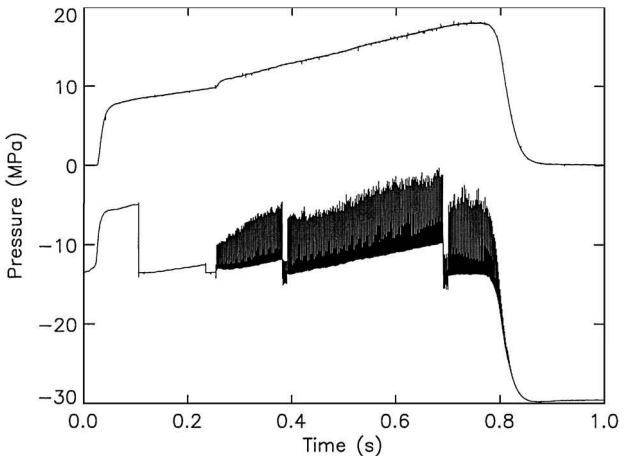

Fig. 1 Experimental example of pulse-triggered instability (top curve: time-averaged; bottom curve: high frequency and shifted by 13 MPa).

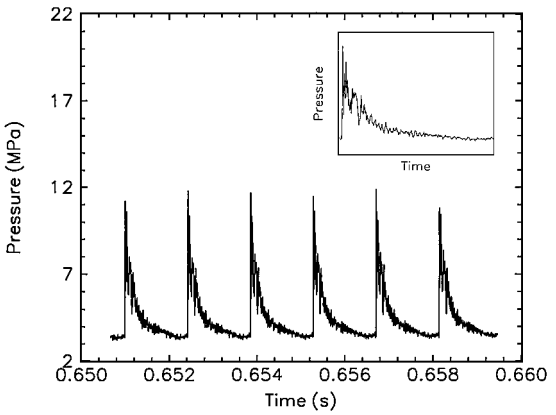

Fig. 2 Train of shock waves from Fig. 1 showing postshock oscillations (inset is for the second cycle).

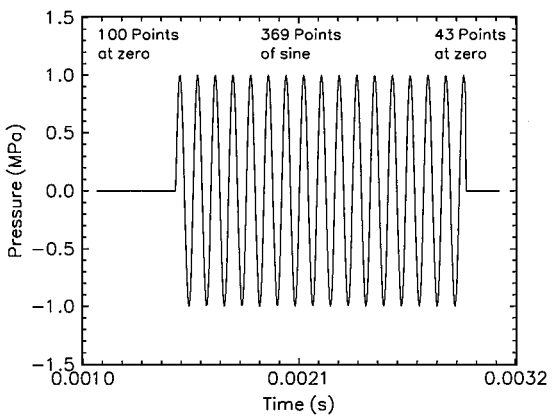

Fig. 3 Model signal 1.

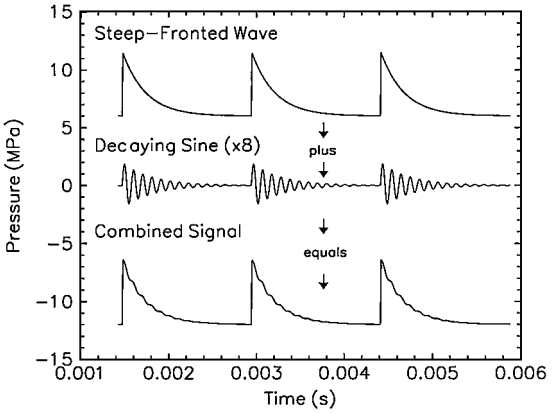

Fig. 4 Model signal 2 (amplitude of the decaying sine increased for readability by a factor of 8).

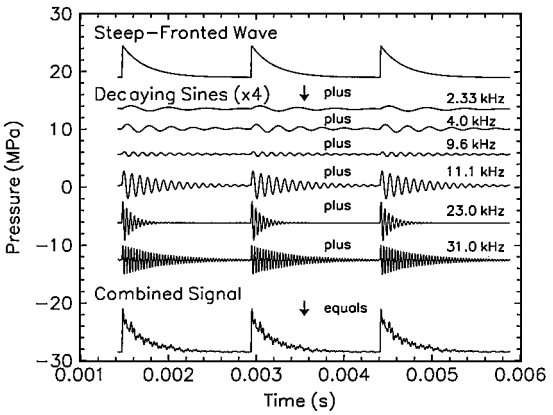

Fig. 5 Model signal 3 (amplitude of the decaying sines increased for readability by a factor of 4).

sine and the combined signal are used throughout this paper in the discussion of the time-marching and the time-frequency components of the new methodology.

Model signal 3, Fig. 5, is a more complex version of model signal 2. It was included to illustrate the effects of a more realistic signal on the behavior of the analyses associated with the new methodology. The frequency and the decay alphas of the six decaying sines are also given in Table 1.

Time-Marching Frequency Analysis

The standard time-marching frequency analysis used in the field of combustion instability was not capable of following the evolution over a motor firing of the frequency content of postshock oscillations. Consequently, a new analysis was developed.

This section begins with a description of the standard analysis. The weaknesses of the standard analysis are then illustrated and the new analysis developed with model signals 2 and 3. Finally, the new analysis is applied to the experimental data in Fig. 1.

Standard Time-Marching Frequency Analysis

The standard time-marching frequency analysis of a pressure signal is based on the calculation of overlapping FFTs. Each consecutive FFT is advanced by a certain percentage of the FFT length. This standard time-marching analysis is illustrated in Figs. 6 and 7. Figure 6 is a 1024-point FFT of the pressure data shown in Fig. 2. With a data sampling rate of 250 ksamples/s and a fundamental longitudinal frequency of 690 Hz, the FFT includes the first 2.8 wave cycles. Figure 7 is composed of a series of 1024-point FFTs of the signal in Fig. 1 with an overlap of 70% and is plotted as a contour plot. The dashed and the solid curves in Fig. 7 approximate the variation with time of the tangential and the radial acoustic-mode frequencies, respectively, of the combustion chamber.

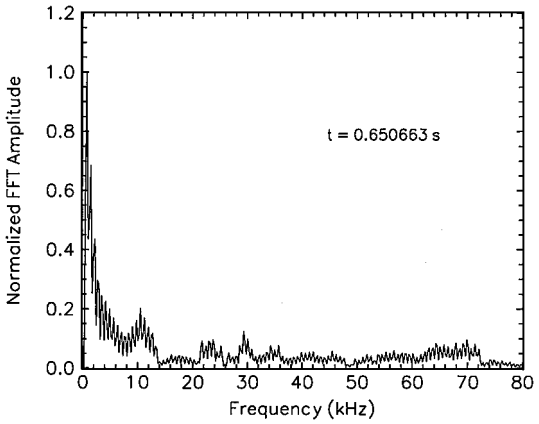

Fig. 6 1024-point FFT of experimental data in Fig. 2.

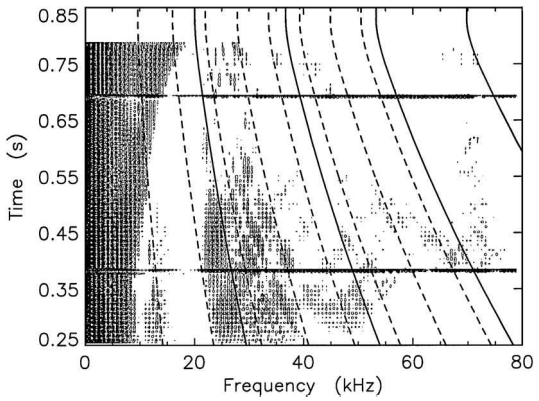

Fig. 7 Contour plot of time-marching 1024-point FFTs for experimental data in Fig. 1 (dashed curves are for tangential modes, and solid curves are for radial modes).

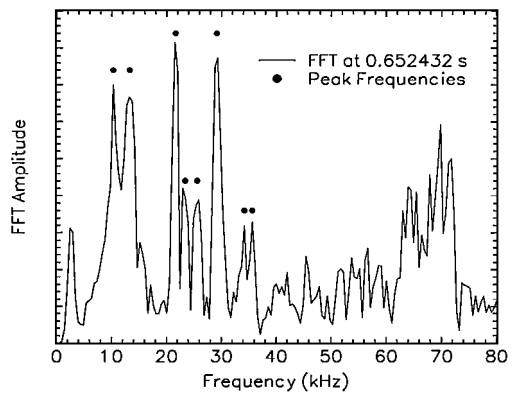

Fig. 8 FFT of a single cycle of the postshock oscillations for the experimental signal in Fig. 2 obtained with the new methodology.

As will be seen in the subsection, Application to the Experimental Data, the frequencies associated with the postshock oscillations generally follow the acoustic frequencies. However, this is not evident from the standard time-marching analysis. Rather, the contours in Fig. 7 tend to be aligned in multiples of the fundamental longitudinal frequency.

The result obtained with the new methodology is shown in Figs. 8 and 9 to facilitate comparison. However, they are not discussed until the subsection, Application to the Experimental Data.

Overcoming the Problems of the Standard Analysis

The standard time-marching frequency analysis has difficulty identifying postshock oscillations for two major reasons. First, the harmonics from the shock wave can mask the presence of other oscillations. Second, the inclusion of multiple cycles in the FFT results in sidelobes at multiples of the fundamental that tend to obscure the actual frequencies in the signal.

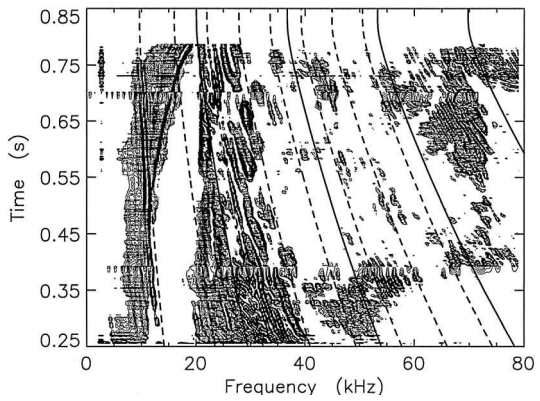

Fig. 9 Contour plot of FFTs of the experimental data in Fig. 1 made with the new methodology (dashed curves are for tangential modes, and solid curves are for radial modes).

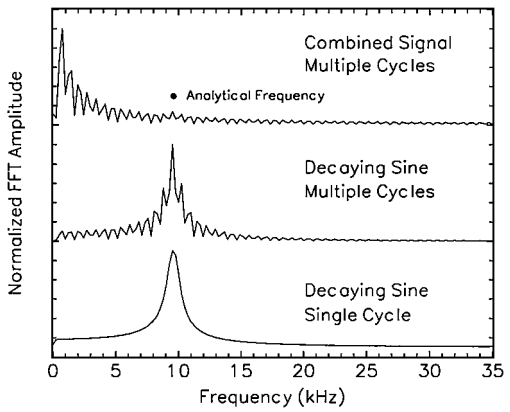

Fig. 10 Problems with the standard time-marching analysis (top two curves) and the proposed solution (bottom curve) illustrated with model signal 2.

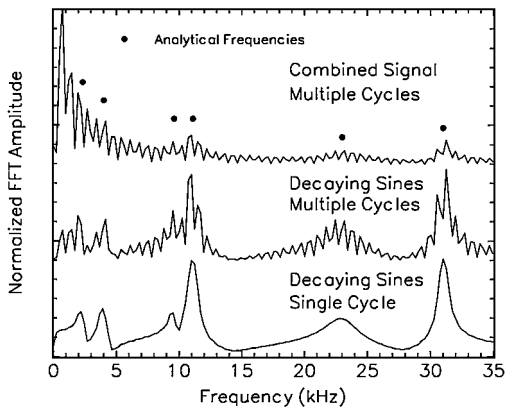

Fig. 11 Problems with the standard time-marching analysis (top two curves) and the proposed solution (bottom curve) illustrated with model signal 3.

The problems with the standard time-marching analysis and their solution are illustrated in Figs. 10 and 11 with the model signals 2 and 3, respectively. Discussion begins with model signal 2, Fig. 10, given its relative simplicity.

The first problem, that of the masking effect of the steep-fronted wave, is illustrated by the curve at the top of Fig. 10 (combined signal multiple cycles). This is the plot of a 1024-point FFT of the combined signal from Fig. 4; the FFT includes 2.8 wave cycles. It is very difficult to identify the frequency peak at 9.6 kHz associated with the decaying sine.

The second problem, that of the effect of including multiple cycles in the analysis, is illustrated in the middle plot of Fig. 10, decaying sine multiple cycles. This is a plot of a 1024-point FFT of the decaying sine from Fig. 4; again the FFT includes 2.8 wave cycles. Here the steep-fronted wave was not present and therefore the individual frequency is much more obvious. However, without previous knowledge of the exact number and frequencies of the sinusoids, in this case only one, the sidelobes at multiples of the fundamental frequency make the actual peak difficult to identify.

The bottom plot of Fig. 10, the decaying sine single cycle, illustrates the result of accounting for the two above-mentioned problems. The FFT for this plot was performed with the first cycle of the decaying sine in Fig. 4, 300 points, with the rest of the 1024-point window filled with zeros. This process is similar to what is illustrated in Fig. 3 for model signal 1. With this analysis the single-frequency peak from the decaying sine is clearly evident. This analysis formed the basis of the new time-marching methodology.

The problems associated with the standard time-marching analysis along with the proposed solution are also illustrated in Fig. 11 for model signal 3. The extra complexity of this signal serves to underline the difficulty of detecting postshock oscillations whose frequencies, in this case 2.33 and 4.0 kHz, approach that of the fundamental shock frequency (see the curve labeled combined signal multiple cycles). It also shows the difficulty in distinguishing two frequencies that are relatively close, in this case 9.6 and 11.1 kHz, from the peaks associated with sidelobes (see the curve labeled decaying sines multiples cycles).

New Time-Marching Analysis

To apply the analysis principles illustrated in the preceding subsection, it was first necessary to remove the train of shock waves from the signal, thereby isolating the postshock oscillations. An algorithm was developed that approximated the shock-wave portion of the signal by first identifying shock peaks and thus wave fronts and then by performing a polynomial fit of the wave tailoff containing the postshock oscillations. The resulting approximate train of shock waves was then subtracted from the original signal, leaving only the postshock oscillations.

The above process is illustrated in Fig. 12 for model signal 2. The combined signal at the top of the figure (from Fig. 4) is the original signal. The shock peaks identified with the algorithm are indicated by the indices in the figure. The polynomial fit produced the middle curve that, when subtracted from the combined signal, produced the resultant signal, the bottom curve. The accuracy of this analysis in the frequency domain is illustrated in Fig. 13, in which the FFT of the first cycle of the decaying sine, from Fig. 4, is compared with that of the first cycle from the resultant signal, Fig. 12. The FFT of the resultant signal is a good approximation of that of the decaying sine. However, the oscillations below 5 kHz for the FFT of the resultant signal indicate potential problems when one is trying to identify postshock oscillations of similar frequencies.

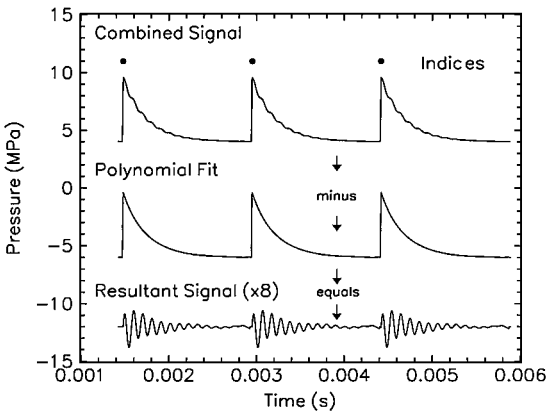

Fig. 12 New methodology applied to model signal 2 (amplitude of the resultant signal increased for readability by a factor of 8).

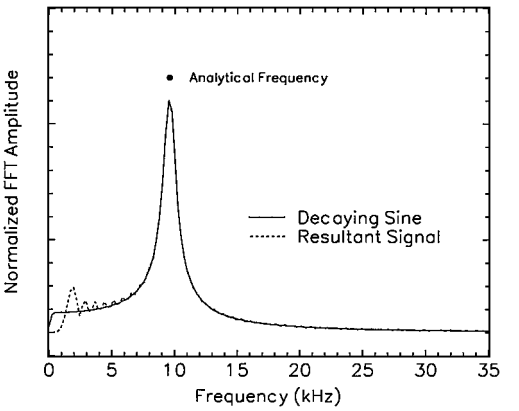

Fig. 13 FFTs of a single cycle of the decaying sine and the resultant signal for model signal 2.

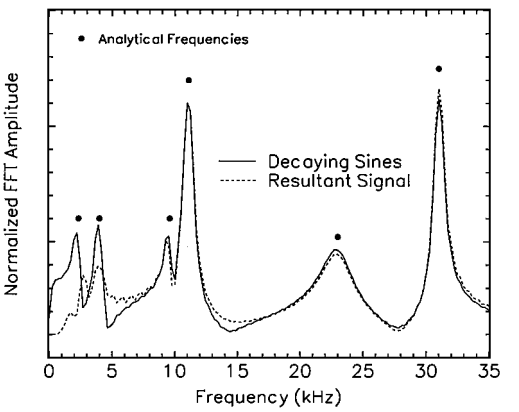

Fig. 14 FFTs of a single cycle of the sum of the decaying sines and the resultant signal for model signal 3.

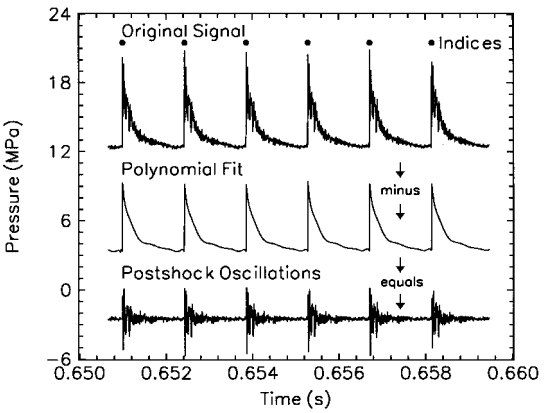

Fig. 15 New methodology applied to the experimental signal in Fig. 2.

The accuracy of the analysis as applied to the more complex model signal 3 is evaluated in the frequency domain in Fig. 14. This example shows a shifting of the lowest frequency, 2.33 kHz, for the resultant signal. In addition, the amplitude of the two lowest-frequency peaks, 2.33 and 4.0 kHz, for the resultant signal is significantly lower than that for the decaying sines.

Application to the Experimental Data

Having demonstrated, with model signals, the advantage of removing the train of shock waves and performing FFTs over single-wave cycles, we applied the analysis to the experimental signal. The removal of the train of shock waves is illustrated in Fig. 15 for the signal from Fig. 2. The original signal is shown at the top of the figure. After identifying the position of the shock peaks (indicated

by the indices in the figure) and performing an eighth-order polynomial regression on the tailoff of each shock cycle, we obtained the approximation of the train of shock waves, the polynomial fit in the middle of the figure. This approximation was then subtracted from the original signal to obtain the postshock oscillations, shown at the bottom of the figure.

An FFT of a single cycle of postshock oscillations beginning at 0.652432 s (from Fig. 15) is shown in Fig. 8. As for the model signals, a single cycle of the experimental signal was composed of only 300 data points. These data points were centered in a 1024-point FFT, 724 of the points being set to zero. For the sampling rate of 250 ksamples/s, the effective frequency resolution of the signal was $\frac{250}{300}$, or 0.83 kHz. Comparison of this FFT with the one based on the standard methodology in Fig. 6 shows the extent to which the new analysis is superior.

The final step in the analysis was to calculate a series of single-cycle FFTs and plot the results as a contour graph. The results of this analysis are plotted as a contour graph in Fig. 9 along with the approximate variation of the tangential and the radial acoustic modes. The results represent a significant improvement over those in Fig. 7 obtained with the standard analysis, in that individual frequencies that follow the global trends of the transverse acoustic modes are readily discernible.

The details of Fig. 9 require interpretation that will be left primarily to subsequent papers. However, three comments are made here. First, the first tangential acoustic mode is identifiable. Second, a series of peaks whose frequency increases with time can be seen between 10 and 18 kHz. This gas chamber oscillation is believed to be stimulated by the first radial-mode vibration of the propellant/casing structure. Its presence was postulated in a previous paper.[5] However, the evidence was not as clear as in this figure. Third, there seems to be significantly more modes of oscillation present in the figure than can be accounted for based on pure transverse-mode oscillations.

Time-Frequency Analysis

The new time-marching frequency analysis follows the evolution, throughout a firing, of the frequency content of postshock oscillations averaged over the decay portion of each shock cycle. However, to describe the behavior of these oscillations completely it is necessary to be able to track the temporal evolution of their frequency content over the decay portions of single cycles. Algorithms that perform this task are the domain of time-frequency analysis.

In the field of digital signal processing, extensive effort has been invested in the development of time-frequency analysis algorithms. At the outset of the present work, several of these algorithms were evaluated for their applicability to the specific problem of tracking the temporal variation of the frequency content of postshock oscillations. The algorithms evaluated were implemented in the MATLAB toolbox by Auger et al.[7,8]

From this initial work, two algorithms were retained as the most promising, the short FFT (SFFT) and the Morlet wavelet transform (MWT). Following an introduction to these algorithms, their frequency resolution is evaluated with model signal 3 and their time resolution is evaluated with all three model signals. Based on these evaluations, the application of the algorithms to one cycle of postshock oscillations, Fig. 15, of the sample experimental signal is discussed.

Introduction to Time-Frequency Analysis

The time-frequency analysis of the first cycle of the decaying sine of model signal 2 (Fig. 4) is illustrated in Fig. 16. The figure shows the decaying sine along with a 129-point Hamming window weighting function (WWF) used in the SFFT analysis and a Morlet wavelet corresponding to a frequency of 35.1 kHz, used for the MWT.

A total of 512 data points was analyzed, 369 points from the decaying sine with the first 100 and last 43 points set equal to zero. The number of points from the decaying sine corresponded to one complete cycle. The total number of points analyzed was chosen as a power of 2.

For the SFFT algorithm, time resolution is obtained through weighting the signal at each time step (data point) with a sliding

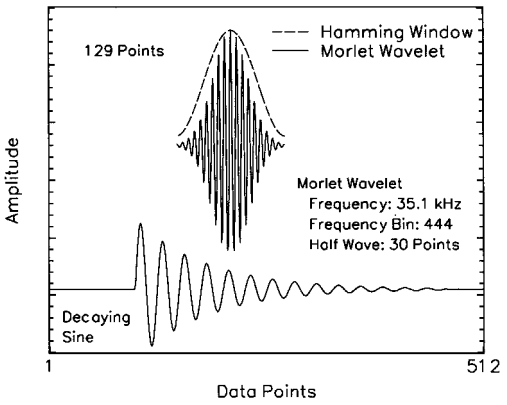

Fig. 16 Illustration of time-frequency analysis for model signal 2.

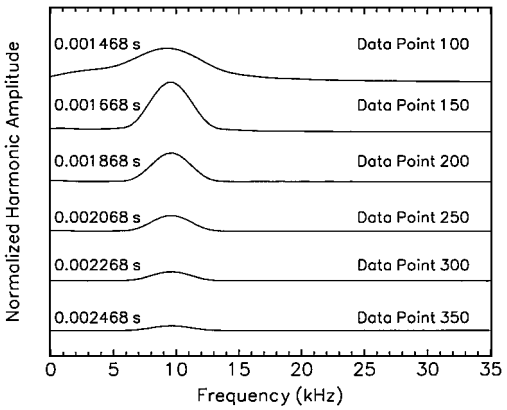

Fig. 17 Evolution with time of the harmonic content of model signal 2 calculated with the SFFT (129, H).

WWF before calculating an FFT. An SFFT analysis results in a series of FFTs, the time (or data point) attributed to a given FFT being that corresponding to the center of the WWF at that step. Selected results from the SFFT analysis of the decaying sine in Fig. 16 are shown in Fig. 17. The time (or data point) markings indicate where the WWF was centered.

The SFFT is based on the convolution of infinite-length sinusoids with a windowed signal. However, for a wavelet transform a signal is convolved with a sliding wavelet of finite length, the baseline wavelet being referred to as the mother wavelet. Each position of the center of the wavelet corresponds to a different time, and through the stretching and compressing of the mother wavelet the different frequencies are investigated. In the field of signal processing many different wavelets have been used. However, for the present analysis a Morlet wavelet was chosen. A 129-point Morlet wavelet is shown in Fig. 16, the oscillations in the wavelet being at a frequency of 35.1 kHz.

In the discussion of the ability of different algorithms to track the temporal variation of the frequency content of postshock oscillations over single cycles, the concepts of time and frequency resolution are of prime importance. However, given the descriptive (as opposed to rigorous mathematics) approach adopted in this discussion, these terms are used loosely throughout the paper. Here, time resolution refers to the general capability of an algorithm to track the temporal evolution of amplitude and frequency resolution refers to the general capability of an algorithm to identify two closely situated frequency peaks. As will be seen in the analysis of model signal 3, time resolution is closely coupled to frequency resolution.

In the discussion of frequency resolution, a distinction needs to be made between the frequency differential involving two consecutive frequency bins, Δf and the effective frequency differential Δf_{eff}. For an SFFT, the value of Δf is a function of the sampling frequency and the length of the FFT; for a 512-point FFT of a signal sampled at 250 kHz, Δf is 488 Hz. Δf_{eff} is a function of the amount of

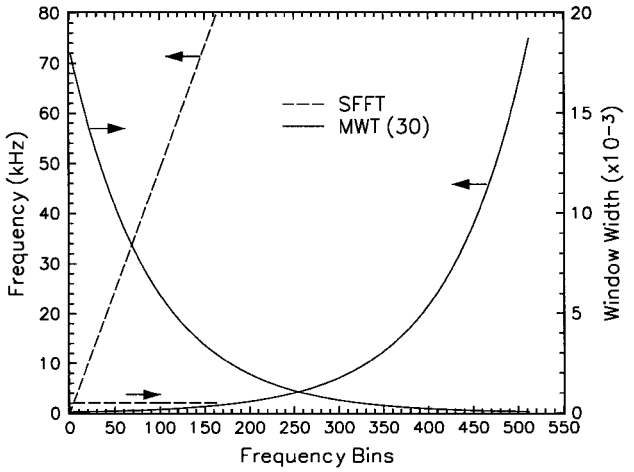

Fig. 18 Relationship between f, Δf $(f_i - f_{i-1})$, window width, and frequency bins for the SFFT and the MWT.

signal analyzed and the length and the shape of the WWF. For a 129-point Hamming WWF (all other points are set to zero) and a sampling rate of 250 kHz, Δf_{eff} is 1940 Hz even if the length of the FFT is 512 points. In practice, frequency resolution is limited by Δf_{eff}.

For the SFFT, time resolution is inversely proportional and frequency resolution is directly proportionalto the length of the WWF, with Δf and Δf_{eff} remaining constant over the frequencies analyzed. This results in conflicting requirements for time and frequency resolution and indicates that any solution to the problem of tracking postshock oscillations involves a compromise.

As for the SFFT, the requirements for time and frequency resolution for the MWT are conflicting. However, for the MWT, the wavelet length (window width) and therefore Δf (and Δf_{eff}) and the time resolution are not constant over the frequencies analyzed. This difference between the MWT and the SFFT is illustrated in Fig. 18. The following comments can be made.

1) Δf for the MWT is not constant as it is for the SFFT. At low frequencies, Δf for the MWT is much smaller than for the SFFT and at high frequencies it is much greater; the variation is logarithmic. For the example shown, Δf for the MWT at 250 Hz was 2.8 Hz and at 75 kHz was 832 Hz, whereas Δf of the SFFT based on a 512-point FFT was constant at 488 Hz.

2) The window width (wavelet length) of the MWT is not constant as it is for the SFFT. At low frequencies the window is much wider than that of the SFFT and at higher frequencies it is much narrower; as for the frequency, the variation is logarithmic. For the example shown, the width of the wavelet at 250 Hz was 18,000 points and at 75 kHz it was 61 points, whereas for the SFFT with the Hamming window it was constant at 129 points.

3) For the MWT, wide windows with small values of Δf at low frequencies and narrow windows with large values of Δf at high frequencies results in good frequency resolution at low frequencies that deteriorates as frequency increases and poor time resolution at low frequencies that improves as frequency increases.

The basic properties of the SFFT and the MWT having been discussed, our goal in the next subsection is to evaluate the implications of these properties for the analysis of postshock oscillations. We accomplish this by applying the algorithms to the three model signals.

Application to Model Signals

With the goal of determining the best methodology for tracking the temporal variation of the frequency content of the postshock oscillations of the experimental signal, we studied the behavior of the time-frequency analysis algorithms by applying them to the three model signals. Frequency resolution is addressed first with the most complex of the signals, model signal 3. Time resolution is then discussed, beginning with model signals 1 and 2 and ending with model signal 3, for which frequency resolution influences time resolution.

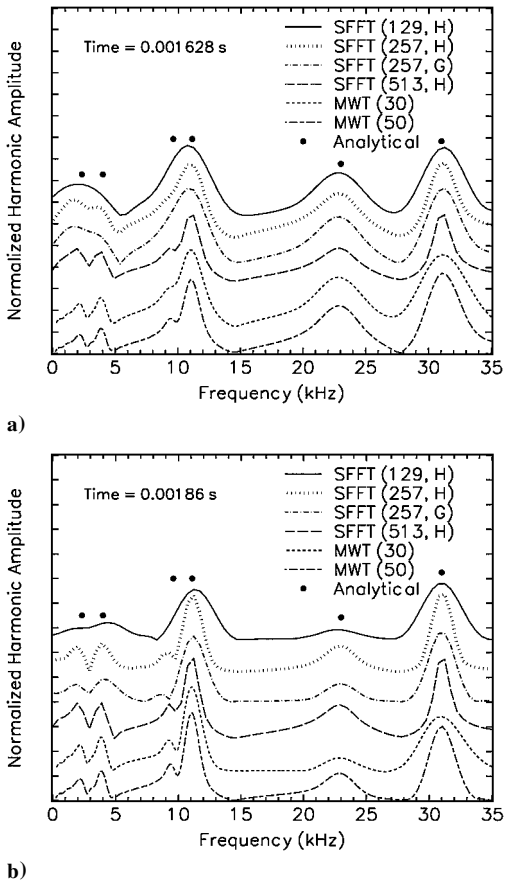

Fig. 19 Effect of algorithm, window width, window type, and time on frequency resolution for model signal 3 (results shifted to increase readability).

Frequency Resolution

The frequency resolution of the time-frequency algorithms was evaluated with the sum of the decaying sines of model signal 3 (Fig. 5) and was shown to depend on algorithm type, WWF width and type, and window (wavelet) width and time.

A sample of the results is shown in Fig. 19. Figure 19a is for analyses centered at 0.001628 s and Fig. 19b is for analyses at 0.00186 s. The analyses included SFFTs with 129-point Hamming (129, H), 257-point Hamming (257, H), 257-point Gauss (257, G), and 513-point Hamming (513, H) WWFs in addition to MWTs with mother wavelets having 30- and 50-point half wavelengths at 75 kHz. The curves in the figure have all been normalized and then shifted to increase the readability of the different characteristics being illustrated.

Figures 19a and 19b illustrate the following characteristics of the frequency resolution of the different analyses:

1) For the SFFTs, the one with the largest WWF (513, H) had the best resolution. In Fig. 19a it was the only SFFT capable of resolving the 9.6-kHz peak.

2) For the SFFTs, the one with the smallest WWF (129, H) had the poorest resolution. In Fig. 19b it was the only SFFT incapable of resolving the 2.33-, 4.0-, and 9.6-kHz peaks.

3) For the SFFTs, the resolution of the Hamming WWF was superior to that of the Gauss WWF. In Fig. 19a (257, H) resolved the 2.33- and 4.0-kHz peaks whereas (257, G) did not.

4) For the MWTs, the one with the largest windows (50) had the best resolution. In Fig. 19a it was the only MWT capable of clearly resolving the 9.6-kHz peak.

5) The resolution of the MWTs was generally superior to that of the SFFTs for the first four peaks in Figs. 19a and 19b. This is where

the widths of the windows of the MWTs were large and the sizes of Δf small.

6) The resolution of the MWTs decreased with frequency to the point that, for the 31-kHz peak, resolution was equivalent to or worse than that of the SFFTs. The base of this peak for the MWT (30), the width of which is inversely proportional to frequency resolution, was wider than all others.

7) The resolution of all analyses tended to improve with time. This is best illustrated by the SFFT (257, G) that at 0.001628 s was incapable of resolving the 2.33-, 4.0-, and 9.6-kHz peaks but capable of resolving them all at 0.00186 s.

In the present discussion, frequency resolution is important to the extent to which it influences the ability of an algorithm to track the temporal evolution of the frequency content of a complex signal. This is pursued during the discussion of model signal 3 in the next subsection.

Time Resolution

The time resolution of the different analyses is addressed in this section first by a discussion of their ability to track a sine wave of constant amplitude, model signal 1. Model signal 2, with its single decaying sine, was the simplest model that resembled the experimental data of interest. Consequently, it was the next signal with which the analyses were evaluated. Finally, the analyses were evaluated against the most complex signal, model signal 3.

The ability of the SFFT and the MWT analyses to track model signal 1 (Fig. 3) is illustrated in Fig. 20a. The results obtained were all normalized to the amplitude of the model signal. The figure shows that there was a delay before the analyses started to track the signal properly and a period at the end of the signal after which tracking was poor. This phenomenon resulted from the finite width of the WWFs and wavelets and as such varied, depending on which was used. It was the SFFT with the smallest WWF, 129 points, that tracked the model signal for the longest period. In addition, the SFFT with the 257-point Gaussian WWF tracked the signal better than the SFFT with the Hamming WWF.

The ability of the SFFT and the MWT algorithms to track the decaying sine of model signal 2 (Fig. 4) is illustrated in Fig. 20b. An inset has been included in the figure to make the results near the end of the signal more readable. The results were all normalized to give the same amplitude as the decaying sine at 0.0022 s. The figure shows the same starting and ending phenomena and dependency on type and width of the WWFs and wavelets as the preceding example. As such, the peak amplitude of model signal 2 was poorly tracked by all of the algorithms, although the SFFT (129, H) showed superior tracking.

The ability of the SFFT and the MWT algorithms to track the sum of the decaying sines of model signal 3 (Fig. 5) is illustrated in Figs. 21a–21f and 22a and 22b. Inserts have been included where necessary to make the results more readable near the end of the signals. In Figs. 21a–21f, the amplitude of the six decaying sines is compared one at a time with the results of the SFFT and the MWT calculations. The ability of the SFFT (257, G) and the MWT (30) to track all six decaying sines is evaluated in Figs. 22a and 22b, respectively. The results obtained from these analyses were normalized such that the sixth frequency, 31.0 kHz, gave the same amplitude as its corresponding decaying sine at 0.0022 s. The figures show the same starting and ending phenomena and dependency on type and width of the WWFs and wavelets as the preceding two examples. However, they have been specifically included to illustrate the following four additional points:

1) For the MWTs, ability to track the amplitude of the decaying sines varied with frequency. It was poorest for the lowest frequency, Fig. 21a, and improved until the highest frequency, Fig. 21f.

2) For the MWTs, the variation in wavelet width with frequency reduced their ability to measure accurately the relative amplitude of signals at different frequencies. The 11.1- and 31.0-kHz decaying sines had identical amplitudes. However, the results obtained for these two frequencies with the MWT (30), Fig. 22b, were significantly different.

3) For the SFFTs, the difficulty discussed in the preceding section of separating the first four frequency peaks resulted in amplitude oscillations and unusually large initial peaks. Oscillations are seen in Figs. 21a–21d for SFFTs with 129 and 257 points. The frequency resolution of the SFFT (513, H) was sufficient to avoid this problem. An unusually large initial peak is shown in Fig. 21c for the SFFT (129, H).

4) The potential for accurately ranking the amplitudes of the different decaying sines varied among the analyses. The best result was obtained with the SFFT (257, G), Fig. 22a, and the worst with the MWT (30), Fig. 22b. After the initial tracking delay mentioned above, the SFFT (257, G) properly ranked the amplitudes of all the decaying sines.

From the above observations it was concluded that no one time-frequency analysis was sufficient to track the temporal variation of the frequency content of postshock oscillations. Rather, a combination of analyses was required, some with superior frequency resolution and some with superior time resolution.

Application to the Experimental Signal

The temporal evolution of the frequency content of the postshock oscillation for a single cycle of the experimental signal in Fig. 15 was tracked with a combination of time-frequency analyses. The SFFT (129, H) and the SFFT (257, G) were used for superior time resolution and the MWT (30) and the MWT (50) were used for superior frequency resolution. The results are shown in Figs. 23a–23d.

The components of the postshock oscillation for which the amplitudes were tracked (Fig. 23) are identified in Fig. 8 as peak frequencies; the figure shows the single-cycle FFT. The frequencies of these components, indicated in the legends of Figs. 23a and 23b, are slightly different from those in Figs. 23c and 23d (i.e., 10.25 kHz for the first component in Fig. 23a and 10.36 kHz in Fig. 23c). These represent variations that are due to the different algorithms, SFFT and MWT, and are treated in the following discussion as the same components.

A detailed discussion of the physical relevance of these analyses will be left to a subsequent paper. However, some cursory remarks are made here.

First, the amplitudes of the majority of the components of the postshock oscillation decrease with time, revealing a possible relationship to the arrival of the shock wave.

Second, the component corresponding in frequency to the first radial mode of vibration of the propellant/casing system, 13.12 kHz, was dominant immediately following the arrival of the shock wave. However, it decayed rapidly to the smallest amplitude. It is believed that the steep-fronted nature of the shock wave stimulated the ringing of the propellant/casing system. These vibrations drove the oscillations of the chamber gas, which decayed with the structural vibrations.

Third, the component corresponding in frequency to the first tangential acoustic mode, 10.36 kHz, was large immediately following the arrival of the shock wave, decreasing rapidly to what appeared to be a finite and constant-amplitude oscillation (Figs. 23a and 23b). A close examination of the MWT (30) and the MWT (50) analyses, which provided high frequency resolution at 10.36 kHz, confirmed that the large amplitude of this oscillation was real and not a numerical distortion resulting from its closeness to the large-amplitude peak at 13.12 kHz. The high initial amplitude of the oscillation implied some relationship to the shock wave, and its continued presence at a lower amplitude implied possible coupling with the combustion process.

Fourth, the amplitude of the 23.37-kHz component showed oscillatory motion after its initial rapid decay (Figs. 23a and 23b). That this was a real oscillation was confirmed from the results of the higher-resolution MWTs (Figs. 23c and 23d) where the oscillation was still present. This behavior begs the question as to the source of the driving energy.

Finally, the component at 25.69 kHz grew toward the middle of the signal and decayed near the end. It did not have the high-amplitude behavior that characterized the other components at the beginning of the signal. Consequently, it was concluded that the relationship

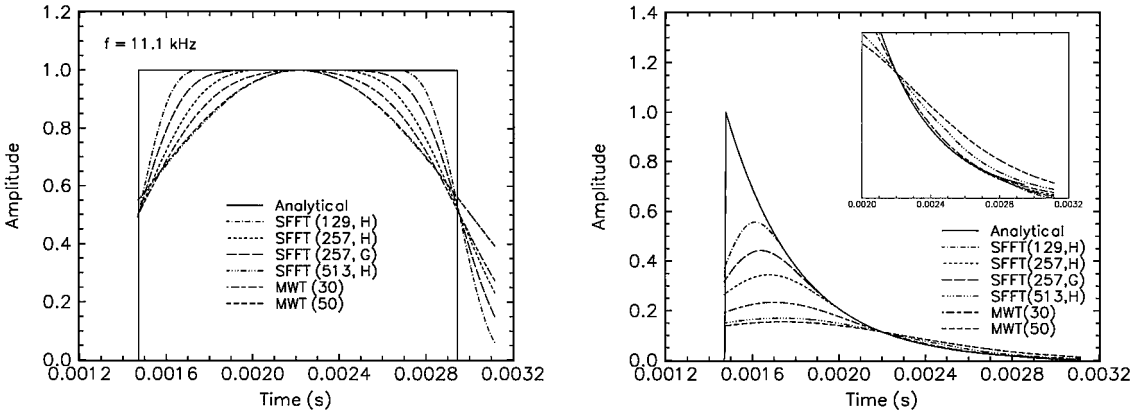

a) b)

Fig. 20 Tracking the temporal evolution of the frequency content of a) model signal 1 and b) model signal 2.

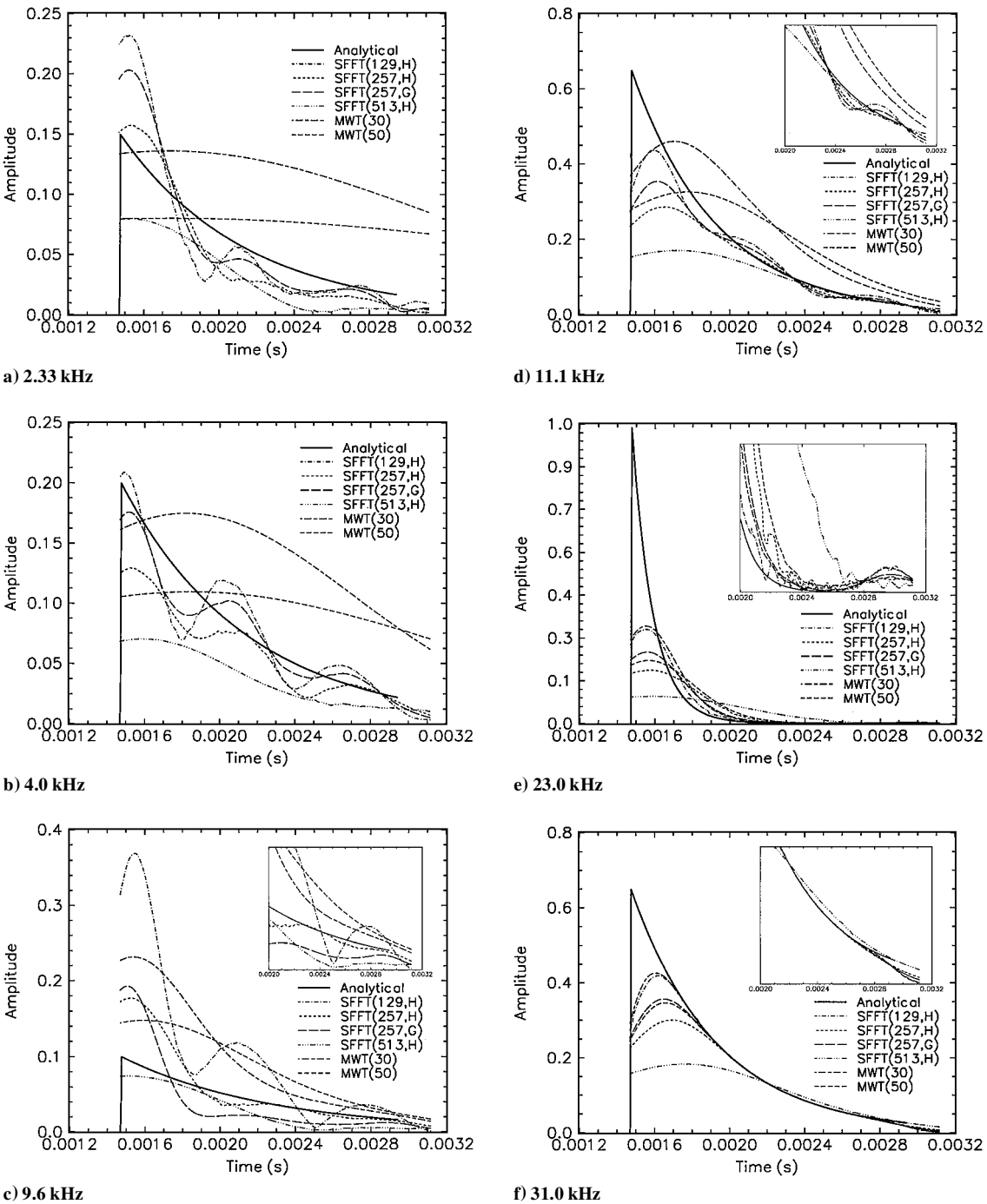

a) 2.33 kHz d) 11.1 kHz

b) 4.0 kHz e) 23.0 kHz

c) 9.6 kHz f) 31.0 kHz

Fig. 21 Tracking the temporal evolution of the frequency content of model signal 3.

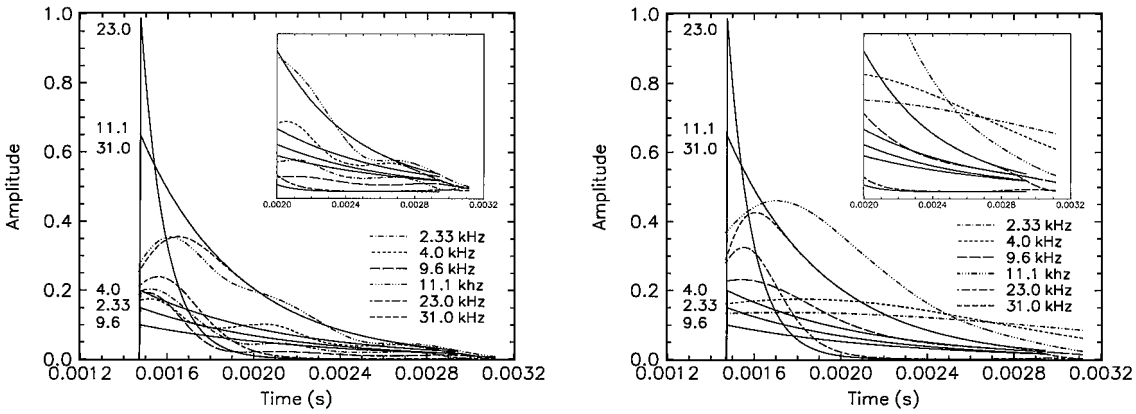

a) SFFT (257, G) b) MWT (30)

Fig. 22 Tracking the temporal evolution of the frequency content of model signal 3.

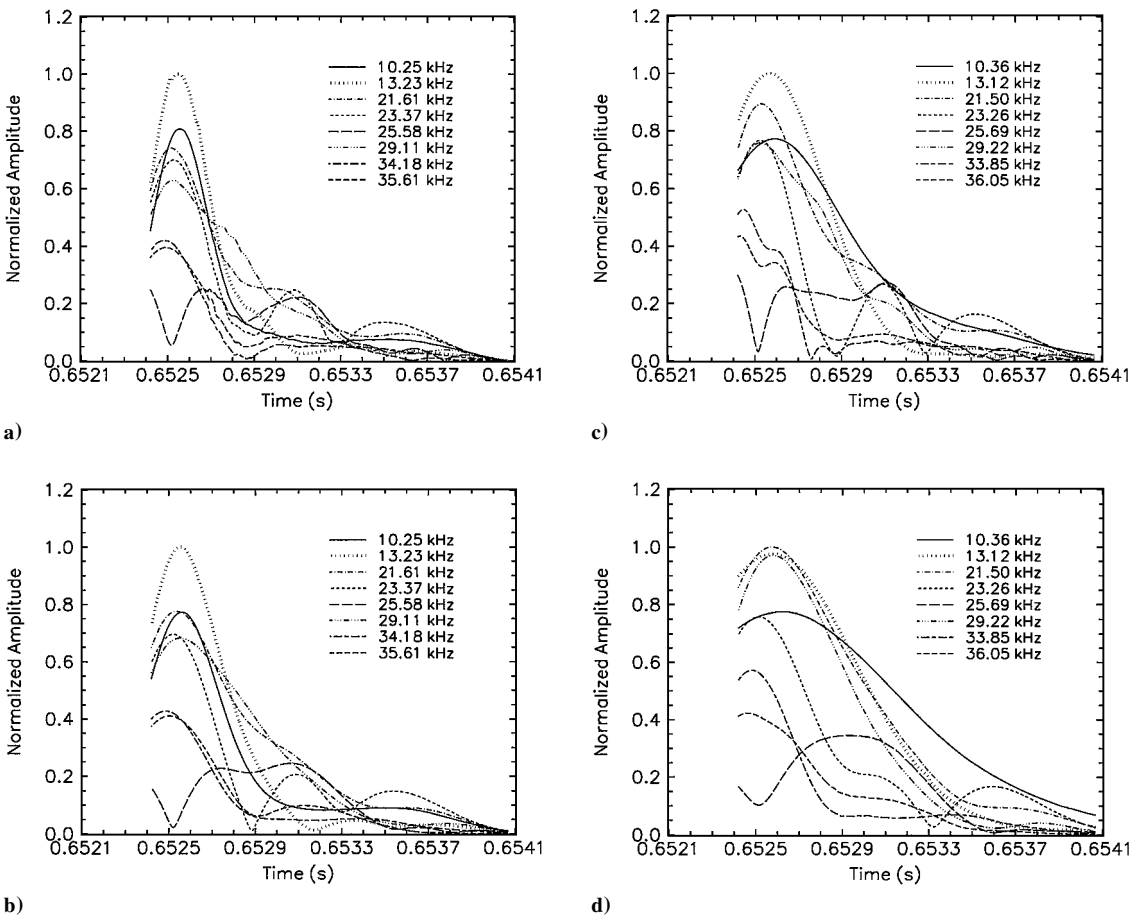

a) c)

b) d)

Fig. 23 Tracking the temporal evolution of the frequency content of the experimental signal in Fig. 2 (inset) by use of a) SFFT (129, H), b) SFFT (257, G), c) MWT (30), and d) MWT (50).

of this component to the arrival of the shock wave was not as direct as that of the other components, if indeed there was a relationship at all.

Conclusions

A new methodology was developed to analyze the postshock oscillations occurring during pulse-triggered instability. This new methodology is composed of a new time-marching frequency and a time-frequency analysis. With the new time-marching analysis it is possible to follow the evolution of the time-averaged frequency content of the postshock oscillations throughout a firing. With the time-frequency analysis it is possible to obtain a qualitative estimate of the temporal evolution of the amplitude of the frequency content of postshock oscillations for a single shock-wave cycle.

It was shown that the standard time-marching frequency analysis used in the field of combustion instability was not capable of following the evolution of the frequency content of postshock oscillations for two reasons. First, the harmonics from the shock wave tend to mask the presence of other oscillations, and second, the sidelobes resulting from including several cycles in a single FFT obscure the actual frequency peaks of a signal. A new analysis, which accounted for these problems, was developed and successfully tested with two model signals.

The new time-marching analysis involved five steps: 1) the identification of the shock peaks throughout the signal, 2) the approximation of the tailoff of the shock waves through polynomial fits, 3) the subtraction of the polynomial fit from the original signal, 4) the calculation of successive single-cycle FFTs with the

previously identified shock peaks as points of reference, and 5) the plotting of the data in the form of a contour graph.

The new analysis was successfully applied to an experimental signal, the results of which showed significant improvement over those obtained with the standard analysis. Multiple frequencies that followed the general trend of the transverse acoustic modes were readily discernible. In addition, a gas chamber oscillation, believed to be stimulated by the first radial mode of vibration of the propellant/casing structure, was also visible.

The performance of two time-frequency analysis algorithms was evaluated with three model signals. The algorithms evaluated were the short fast Fourier transform and the Morlet wavelet transform. The evaluation included the effect of width and type of window weighting functions and width of the mother wavelet. The goal was to identify an analysis or combination of analyses that could be used to track the temporal evolution of the amplitude of the frequency content of postshock oscillations for a single shock-wave cycle. The evaluation, based on the model signals, indicated that no single algorithm was sufficient for the task.

The following overall observations were made concerning the performance of the analyses: 1) The finite width of the WWFs and wavelets resulted in poor tracking at the beginning and the end of all analyses, 2) WWF and wavelet width and WWF type had a significant effect on the time resolution of a given analysis, 3) the time resolution of the MWTs varied with frequency, 4) the variation in wavelet width with frequency reduced the ability of MWTs to measure accurately the relative amplitude of signals at different frequencies, 5) the poor frequency resolution of certain SFFTs resulted in amplitude oscillations and unusually large initial peaks, and 6) the potential for accurately ranking the amplitudes of the different components varied among the analyses.

Based on the above observations, a combination of four analyses was successfully applied to an experimental signal. The analyses included the SFFT (129, H) and the SFFT (257, G) for superior time resolution and the MWT (30) and the MWT (50) for superior frequency resolution. These analyses revealed that the majority of the oscillatory components of the experimental signal decreased with time, indicating a possible relationship to the arrival of the shock wave.

The development of a new methodology for the analysis of postshock oscillations has set the stage for a detailed study of their nature and source. This will be treated in future publications.

References

[1]Brownlee, W. G., "Nonlinear Axial Combustion Instability in Solid Propellant Motors," *AIAA Journal*, Vol. 2, No. 2, 1964, pp. 275–284.

[2]Harris, P. G., and de Champlain, A., "Experimental Database Describing Pulse-Triggered Nonlinear Instability in Solid Rocket Motors," *Journal of Propulsion and Power*, Vol. 14, No. 4, 1998, pp. 429–439.

[3]Baum, J. D., Levine, J. N., and Lovine, R. L., "Pulsed Instabilities in Rocket Motors: A Comparison Between Predictions and Experiments," *Journal of Propulsion and Power*, Vol. 4, No. 4, 1988, pp. 308–316.

[4]Blomshield, F. S., Mathes, H. B., Crump, J. E., Beiter, C. A., and Beckstead, M. W., "Nonlinear Stability Testing of Full-Scale Tactical Motors," *Journal of Propulsion and Power*, Vol. 13, No. 3, pp. 356–366.

[5]Harris, P. G., Wong, F. C., and de Champlain, A., "The Influence of Structural Vibrations on Pulse-Triggered Nonlinear Instability in Solid Rocket Motors: An Experimental Study," AIAA Paper 96-3250, July 1996.

[6]Harris, P. G., de Champlain, A., and Bourque, C., "Pulse-Triggered Nonlinear Instability in Solid Rocket Motors: An Experimental Study," AIAA Paper 97-3246, July 1997.

[7]Auger, F., Flandrin, P., Gonçalvès, P., and Lemoine, O., "Time-Frequency Toolbox: Tutorial," Centre National de la Recherche Scientifique, Paris, and Rice Univ., Houston, TX, 1995–1996.

[8]Auger, F., Flandrin, P., Gonçalvès, P., and Lemoine, O., "Time-Frequency Toolbox: Reference Guide," Centre National de la Recherche Scientifique, Paris, and Rice Univ., Houston, TX, 1995–1996.